






Dual-Side Capacitor Tuning and Cooperative Control for Efficiency-Optimized Wide Output Voltages in Wireless EV Charging

Gangwei Zhu , Graduate Student Member, IEEE, Jianning Dong , Senior Member, IEEE, Thiago Batista Soeiro , Senior Member, IEEE, Hani Vahedi , Senior Member, IEEE, and Pavol Bauer , Senior Member, IEEE

Abstract—This article presents a dual-side capacitor tuning and cooperative control strategy for wireless electric vehicle (EV) charging. To improve the efficiency of wireless EV charging across broad output voltages and wide-range load variations, this article introduces a reconfigurable WPT system by incorporating two switch-controlled-capacitors (SCCs) into the double-sided LCC (DLCC) compensation network. Based on the analytical model of the system, optimal capacitor tuning factors are derived to reduce the rms values of the inductor currents and to minimize the turn-OFF currents across the semiconductors. Furthermore, a dual-side cooperative control strategy is proposed. Through the collaborative control of the inverter, rectifier, and SCCs, the proposed method achieves dual-side optimal zero-voltage-switching (ZVS), wide power regulation, and maximum efficiency tracking simultaneously. Compared with the existing triple-phase-shift (TPS) method, the proposed approach improves the system efficiency across a wide range of dc output voltages and power levels. Experimental results demonstrate that the proposed method achieves a maximum efficiency improvement of up to 1.8% in the boost mode and 1.9% in the buck mode.

Index Terms—Capacitor tuning, dual-side control, electric vehicles (EVs), wireless charging.

I. INTRODUCTION

EXTENSIVE research efforts have been dedicated to wireless power transfer (WPT) technology, primarily owing to its capability to eliminate the constraints associated with conventional physical cables. This technology holds great promise

Manuscript received 2 January 2024; revised 30 April 2024 and 18 June 2024; accepted 24 July 2024. Date of publication 19 August 2024; date of current version 14 February 2025. This work was supported by the China Scholarship Council (CSC) under Grant 202106230112. (Corresponding author: Gangwei Zhu.)

Gangwei Zhu, Jianning Dong, Hani Vahedi, and Pavol Bauer are with the DC System, Energy Conversion and Storage Group, Faculty of Electrical Engineering, Mathematics and Computer Science, Delft University of Technology, 2624 Delft, The Netherlands (e-mail: g.zhu-2@tudelft.nl; j.dong-4@tudelft.nl; h.vahedi@tudelft.nl; p.bauer@tudelft.nl).

Thiago Batista Soeiro is with the Faculty of Electrical Engineering, Mathematics and Computer Science, University of Twente, 7522 Enschede, The Netherlands (e-mail: t.batistasoeiro@utwente.nl).

Digital Object Identifier 10.1109/TIE.2024.3436666

TABLE I
BATTERY VOLTAGES OF SEVERAL EV MODELS IN THE MARKET [5], [6]

Manufacturer	EV Model	Battery Voltage	Year of Release
Tesla	Cybertruck	816 V	2024
Tesla	Model S	400 V	2023
Tesla	Model 3	360 V	2023
Volkswagen	ID.4	408 V	2023
Hyundai	IONIQ 6	800 V	2023
KIA	EV6	697 V	2023
BMW	i4	398 V	2023
BMW	i7	376 V	2023
Porsche	Taycan	800 V	2023
Mercedes-benz	EQS	500 V	2022
Mercedes-benz	EQB	420 V	2022
Audi	e-tron	396 V	2022

for electric vehicle (EV) charging, particularly with the advent of autonomous driving. However, widespread promotion for wireless EV charging still faces several challenges, one of which is addressing drivers' concerns about charging efficiency [1].

Apart from optimizing coil design to push the boundaries of wireless charging efficiency [2], numerous researchers are also engaged in enhancing efficiency over a wide operating range. There are two important factors resulting in a wide operating range [3]. First, the equivalent EV battery load experiences significant fluctuations during the charging process, resulting in substantial variations in charging power. Second, the system also needs to effectively manage wide output voltages, with one of the reasons being the variation in battery voltage while charging. Moreover, given the increasing variety of EV models in the market, it is noteworthy that their nominal battery voltages are inconsistent, as shown in Table I. Hence, it is important for the system to accommodate various battery voltages, thus enabling interoperability and efficient charging for diverse EVs [4].

An intuitive circuitry solution for accommodating a wide operating range is to incorporate dc–dc converters in the front-and/or back-end of the system [7], [8]. However, the introduction of dc–dc converters leads to increased losses, higher costs, and reduced power density [8].

Another effective method for achieving wide-range operation aims to optimize modulation and control strategies for the inverter and/or rectifier of the system. Existing control strategies for the WPT system can be generally categorized into three groups: primary-side control [9], secondary-side control [10], and dual-side cooperative control [11]. Compared with single-side control, dual-side control significantly expands the operating range by replacing the passive diode rectifier with an active rectifier. Implementing this circuitry, Huang et al. proposed a dual-phase-shift (DPS) control strategy in [12], where the phase-shift angles of the inverter and rectifier were adjusted cooperatively to achieve power regulation and optimal load tracking. However, the DPS method encounters hard switching under wide-range load fluctuations. To address this problem, Zhang et al. introduced the phase difference of the dual-side ac voltages as a new control freedom to facilitate zero-voltage-switching (ZVS) [13]. This method is known as triple-phase-shift (TPS) control. Although the existing TPS method is able to achieve wide power regulation and ZVS, it leads to remarkably increased reactive power when the output voltage varies significantly. A detailed demonstration of this point of view will be elaborated in Section II-B. Based on the TPS method, the hybrid modulation strategy was further proposed in [14] and [15], where the half-bridge (HB) mode was introduced to improve the efficiency under light-load conditions; however, it does not improve efficiency as the output power approaches the rated level. Additionally, the hybrid modulation fails to effectively address the issue of efficiency drop when the output voltage varies significantly. Existing dual-side control methods lack effective measures to simultaneously address wide power regulation and wide output voltage variations while maintaining high efficiency.

To fill up the above research gap, this article proposes a dual-side cooperative control strategy based on a reconfigurable double-sided LCC (DLCC) compensation network. The DLCC topology achieves load-independent constant-current (CC) output and provides increased design flexibility, which has been widely investigated in wireless EV charging [16], [17], [18]. Based on the DLCC network, this article incorporates two separate switched-controlled-capacitors (SCCs) on the primary and secondary sides, respectively. The SCC technique has been extensively studied for WPT systems. To deal with the inductance variations caused by substantial coil misalignment, the SCC technique proves effective by dynamically compensating for the varying inductances [19], [20], [21]. Additionally, the SCC method can also be employed to achieve wide ZVS. In [22], a primary-side SCC was integrated into the LCC-S topology to achieve wide inverter ZVS. Moreover, Zhou et al. integrated a secondary-side SCC for the DLCC topology to minimize the input current of the rectifier [23]. It is noteworthy that the methods presented in [22] and [23] only consider the primary-side control. Nevertheless, the operating range of the primary-side

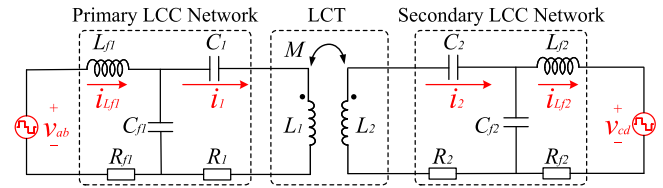


Fig. 1. Equivalent model of the traditional DLCC-compensated system.

control is limited. To extend the operating scope, Fu et al. further implemented the secondary-side SCC with dual-side control [24]. Although the operating range is effectively expanded, this approach only improves the efficiency in the buck mode, and therefore, the efficiency-optimized output voltage range is constrained. Considering the limitations of previous research, a dual-side cooperative control strategy is proposed in this article, and the main contributions of this work are as follows.

- 1) A reconfigurable DLCC topology is introduced, featuring two SCCs integrated on the primary and secondary sides, respectively. Moreover, detailed system characteristics under dual-side capacitor tuning are investigated.
- 2) An analytical model for the reconfigurable DLCC topology is established. Based on this model, optimal capacitor tuning factors are derived to mitigate the reactive power, thereby reducing the inductor rms currents and minimizing the turn-OFF currents for the H-bridge converters.
- 3) A dual-side capacitor tuning and cooperative control strategy is proposed. Through the cooperative control of the inverter, rectifier, and SCCs, the proposed strategy achieves dual-side optimal ZVS, wide output power regulation, and maximum efficiency tracking simultaneously. Notably, this approach improves efficiency in both the buck and boost modes, enabling efficient charging for a broad range of output power and accommodating significant output voltage variations.

The remainder of this article is structured as follows. Section II highlights the limitations of conventional methods and introduces the proposed reconfigurable DLCC topology with dual-side SCCs. Moreover, Section III elaborates on the proposed dual-side capacitor tuning and cooperative control strategy, while Section IV presents the experimental results. Finally, the conclusions of this article are given in Section V.

II. PROPOSED RECONFIGURABLE DLCC-COMPENSATED WPT SYSTEM WITH DUAL-SIDE SCCS

A. Conventional DLCC-Compensated WPT System

Fig. 1 presents the equivalent circuit model for the conventional DLCC-compensated WPT system. In this diagram, v_{ab} and v_{cd} indicate the ac voltages generated by the inverter and rectifier, respectively. The wireless coils are regarded as a loosely coupled transformer (LCT), where L_1 is the primary self-inductance, L_2 is the secondary self-inductance, and M is the mutual inductance. To enhance the power factor of the system, both the primary and secondary sides of the LCT are compensated using the LCC networks. The DLCC topology

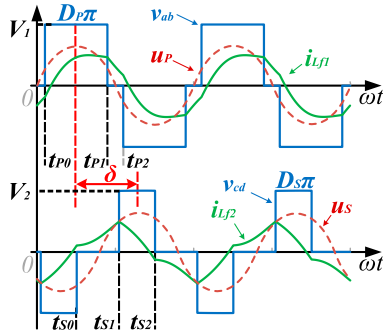


Fig. 2. Typical operating waveforms of the conventional TPS control.

is designed as: $L_{f1}C_{f1} = 1/\omega_n^2$, $L_{f2}C_{f2} = 1/\omega_n^2$, $L_1 - L_{f1} = 1/(\omega_n^2 C_1)$, and $L_2 - L_{f2} = 1/(\omega_n^2 C_2)$, where ω_n represents the nominal resonant frequency.

Moreover, to achieve power regulation and implement ZVS, the TPS control is commonly adopted. Fig. 2 presents the typical operating waveforms of the existing TPS method. In Fig. 2, V_1 and V_2 are the dc input and output voltages, while u_P and u_S represent the fundamental components of v_{ab} and v_{cd} , respectively. Additionally, the inverter and rectifier duty cycles are denoted by D_P and D_S , while the phase difference between u_P and u_S is indicated by δ . According to [13], when employing the TPS control, the transfer efficiency of the resonant circuits is approximated as

$$\eta \approx \omega M L_{f1} L_{f2} |\sin(\delta)| \times [(R_2 L_{f1}^2 + M^2 R_{L_{f1}}) G_{AC} + (R_1 L_{f2}^2 + M^2 R_{L_{f2}}) / G_{AC} + \omega M L_{f1} L_{f2} |\sin(\delta)|]^{-1} \quad (1)$$

where $G_{AC} = |\dot{U}_S|/|\dot{U}_P|$ represents the ac voltage gain of the resonant circuits; and $|\dot{U}_P|$ and $|\dot{U}_S|$ indicate the rms values of u_P and u_S , which are given by

$$|\dot{U}_P| = \frac{2\sqrt{2}V_1}{\pi} \sin\left(\frac{D_P\pi}{2}\right), |\dot{U}_S| = \frac{2\sqrt{2}V_2}{\pi} \sin(D_S\pi/2). \quad (2)$$

As evident from (1), to realize maximum efficiency tracking for the resonant circuits, the inverter and rectifier duty cycles should be adjusted as

$$\frac{\sin(D_S\pi/2)}{\sin(D_P\pi/2)} = \frac{V_1}{V_2} \sqrt{\frac{bR_1 + cR_{L_{f2}}}{R_2/b + cR_{L_{f1}}}} \quad (3)$$

where $b = L_{f2}/L_{f1}$, $c = M^2/(L_{f1}L_{f2})$. Moreover, to achieve ZVS in the TPS control, the phase angle δ needs to be modified away from $\pi/2$. For convenience of analysis, the phase angle δ is expressed as $\delta = \pi/2 + \Delta\delta$, where $\Delta\delta$ represents the compensation angle for enabling ZVS. Increasing $\Delta\delta$ allows for greater injection of reactive power into the resonant circuits, consequently achieving ZVS for the inverter and rectifier. Specifically, the minimum value of $\Delta\delta$ for achieving the inverter ZVS is determined as

$$\Delta\delta_P = \arccos \left\{ \frac{1}{8MV_2\sin(D_S\pi/2)} \times [-2\pi\omega L_{f1}L_{f2}I_{ZVS} + V_1L_{f2}(D_P\pi^2 - 8\sin^2(D_P\pi/2))] \right\} - D_P\pi/2 \quad (4)$$

TABLE II
SYSTEM PARAMETERS OF THE INVESTIGATED WPT SYSTEM

Symbol	Parameters	Value	Unit
M	Mutual inductance	95.0	μH
L_1, L_2	Coil inductances	335.8, 224.7	μH
C_1, C_2	Series capacitances	14.8, 25.3	nF
C_{f1}, C_{f2}	Parallel capacitances	33.1, 41.3	nF
L_{f1}, L_{f2}	Compensation inductances	103.8, 83.8	μH
R_1, R_2	Coil resistances	0.45, 0.30	Ω
$R_{L_{f1}}, R_{L_{f2}}$	Inductor resistances	0.20, 0.14	Ω
V_1	DC input voltage	300	V
V_2	DC output voltage	150–450	V
f_s	Resonant frequency	85	kHz

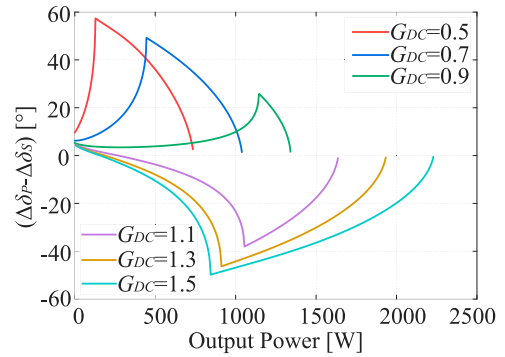


Fig. 3. Difference between $\Delta\delta_P$ and $\Delta\delta_S$ under various output power and voltages. Here, $G_{DC} = V_2/V_1$ is the dc voltage gain of the system.

where I_{ZVS} is the threshold current for charging/discharging C_{oss} of the power switches within the dead time. Similarly, the minimum value of $\Delta\delta$ for the rectifier ZVS is as follows:

$$\Delta\delta_S = \arccos \left\{ \frac{1}{8MV_1\sin(D_P\pi/2)} \times [-2\pi\omega L_{f1}L_{f2}I_{ZVS} + V_2L_{f1}(D_S\pi^2 - 8\sin^2(D_S\pi/2))] \right\} - D_S\pi/2. \quad (5)$$

Finally, to ensure ZVS for both the inverter and rectifier, the compensation angle $\Delta\delta$ is selected as

$$\Delta\delta = \max(\Delta\delta_P, \Delta\delta_S). \quad (6)$$

B. Limitations in Wide Output Voltage Applications

To accommodate diverse EV models in the market, it is advantageous for the WPT systems to efficiently manage broad output voltages. However, the existing TPS method exhibits significant limitations when the output voltage varies.

When the system needs to manage wide output voltages, as indicated in (3), it becomes necessary to regulate the duty cycles D_P and D_S in an inconsistent manner to achieve maximum efficiency tracking. Further examination of (4) and (5) reveals that the difference between the compensation angles $\Delta\delta_P$ and $\Delta\delta_S$ also undergoes significant variations as the output voltage and power change. With the system parameters listed in Table II, the distinction between $\Delta\delta_P$ and $\Delta\delta_S$ under various output power and voltages is illustrated in Fig. 3. Therein, the

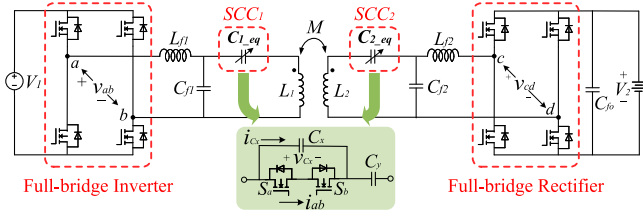


Fig. 4. Topology of the proposed reconfigurable DLCC-compensated system with dual-side SCCs. Herein, C_{1_eq} and C_{2_eq} represent the equivalent capacitance of the primary and secondary SCC, respectively.

disparity between $\Delta\delta_P$ and $\Delta\delta_S$ initially rises with increasing output power and subsequently exhibits a decrease as the power approaches the rated level. Another notable point is that this difference becomes more pronounced as the dc voltage gain deviates from the unity value.

As described in (6), the existing TPS control selects the maximum value of $\Delta\delta_P$ and $\Delta\delta_S$ to guarantee ZVS for both the inverter and rectifier. However, when the difference between $\Delta\delta_P$ and $\Delta\delta_S$ becomes significant, this approach results in increased reactive power. Taking $G_{DC} = 0.5$ as an example, the value of $\Delta\delta_P$ exceeds that of $\Delta\delta_S$, and this difference becomes significant under power variations. This implies that even though ZVS for the rectifier can be achieved at $\Delta\delta = \Delta\delta_S$, the compensation angle $\Delta\delta$ must be selected as $\Delta\delta_P$ to ensure ZVS for the inverter, which leads to extra reactive power on the secondary side. The presence of this excessive reactive power results in increased currents, consequently reducing the system's efficiency.

C. Proposed Reconfigurable System With Dual-Side SCCs

To reduce the above-mentioned additional reactive power, a reconfigurable DLCC-compensated WPT system is introduced, as shown in Fig. 4. This system incorporates two separate SCCs, one configured on the primary side and the other on the secondary side. The implementation of dual-side SCCs allows for continuous tuning for the equivalent capacitances of C_{1_eq} and C_{2_eq} . Distinct from the conventional DLCC network, the proposed system operates at detuned conditions. For ease of analysis, the detuning factors of the primary (α) and secondary (β) resonant circuits are denoted by

$$\alpha = \frac{\omega L_1 - 1/(\omega C_{1_eq})}{X_1}, \beta = \frac{\omega L_2 - 1/(\omega C_{2_eq})}{X_2} \quad (7)$$

where $X_1 = \omega L_{f1}$ indicates the primary characteristic reactance, while $X_2 = \omega L_{f2}$ represents the secondary characteristic reactance. Furthermore, using the fundamental harmonic analysis (FHA) method and ignoring the loss resistances, the circuit model of the proposed system is simplified, as shown in Fig. 5. Here, \dot{U}_P , \dot{U}_S , \dot{I}_1 , \dot{I}_2 , $\dot{I}_{L_{f1}}$, and $\dot{I}_{L_{f2}}$ are the phasor forms of the fundamental components of v_{ab} , v_{cd} , i_1 , i_2 , $i_{L_{f1}}$, and $i_{L_{f2}}$, respectively. Based on this simplified model, the basic characteristics of the system are analyzed as follows.

1) *Coil Currents*: Based on Fig. 5 and applying Kirchhoff's voltage law (KVL), expressions of \dot{I}_1 and \dot{I}_2 are derived as

$$\dot{I}_1 = -j\dot{U}_P/X_1, \dot{I}_2 = j\dot{U}_S/X_2. \quad (8)$$

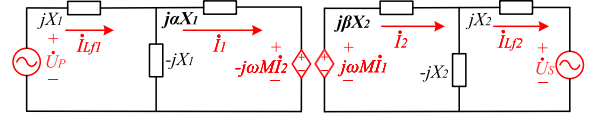


Fig. 5. Simplified equivalent circuit model of the proposed system.

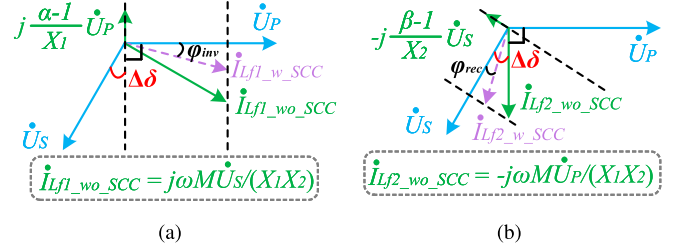


Fig. 6. Impact of (a) primary and (b) secondary SCC tuning on ZVS. Here, $\dot{I}_{L_{f1_w_SCC}}$ and $\dot{I}_{L_{f1_wo_SCC}}$ indicate the primary inductor current with and without SCC tuning, while $\dot{I}_{L_{f2_w_SCC}}$ and $\dot{I}_{L_{f2_wo_SCC}}$ represent the secondary inductor current with and without SCC tuning.

As evident from (8), the coil currents \dot{I}_1 and \dot{I}_2 are only determined by the excited ac voltages \dot{U}_P and \dot{U}_S , as well as the characteristic reactances X_1 and X_2 . Adjusting the detuning factors α and β does not influence the coil currents.

2) *Inductor Currents*: Moreover, the inductor currents $\dot{I}_{L_{f1}}$ and $\dot{I}_{L_{f2}}$ are derived as

$$\dot{I}_{L_{f1}} = j\frac{\alpha-1}{X_1}\dot{U}_P + j\frac{\omega M}{X_1 X_2}\dot{U}_S \quad (9)$$

$$\dot{I}_{L_{f2}} = -j\frac{\beta-1}{X_2}\dot{U}_S - j\frac{\omega M}{X_1 X_2}\dot{U}_P. \quad (10)$$

As indicated by (9) and (10), both the amplitudes and the phase angles of $\dot{I}_{L_{f1}}$ and $\dot{I}_{L_{f2}}$ can be adjusted by modifying α and β . It is noteworthy that tuning α solely influences $\dot{I}_{L_{f1}}$, whereas adjusting β exclusively impacts $\dot{I}_{L_{f2}}$. This unique characteristic allows for independent control of $\dot{I}_{L_{f1}}$ and $\dot{I}_{L_{f2}}$ through separate adjustments of α and β .

3) *Output Power*: The output power of the proposed system is derived as

$$P_{out} = \text{Re}\{\dot{U}_S \dot{I}_{L_{f2}}^*\} = \frac{M}{\omega L_{f1} L_{f2}} |\dot{U}_P| |\dot{U}_S| \sin(\delta). \quad (11)$$

As shown in (11), the system output power remains unaffected by the values of α and β , indicating that dual-side capacitor tuning has little impact on the output power.

4) *ZVS Analysis*: To investigate how to achieve ZVS, the phasor diagrams of the voltages and currents under dual-side SCC tuning are illustrated in Fig. 6. Here, φ_{inv} is the phase difference between \dot{U}_P and $\dot{I}_{L_{f1}}$, while φ_{rec} is the phase difference between \dot{U}_S and $\dot{I}_{L_{f2}}$. As shown in Fig. 6, with the compensation angle $\Delta\delta$ raises, the phase angles φ_{inv} and φ_{rec} increase accordingly, facilitating ZVS for both the inverter and rectifier. Nonetheless, based on the analysis in Section II-B, this approach leads to excessive reactive power at wide output voltages. Fortunately, as indicated by Fig. 6, adjusting α and β allows for the reduction of φ_{inv} and φ_{rec} , as well as $I_{L_{f1}}$

and I_{Lf2} . Consequently, when $\Delta\delta$ is selected as the maximum value of $\Delta\delta_P$ and $\Delta\delta_S$ for dual-side ZVS, it is feasible to further regulate α or β to minimize excessive reactive power. Details on how to optimize the values of α and β are shown in Section III-A.

III. PROPOSED STRATEGY FOR DUAL-SIDE CAPACITOR TUNING AND COOPERATIVE CONTROL

A. ZVS With Minimum Reactive Power

According to [13], to achieve ZVS while minimizing reactive power, the following conditions should be satisfied:

$$i_{Lf1}(t_{P0}) = -I_{ZVS}, i_{Lf2}(t_{S2}) = -I_{ZVS}. \quad (12)$$

As shown in (12), to achieve optimal ZVS, it is imperative to derive the time-domain expressions for the inductor currents i_{Lf1} and i_{Lf2} . Although the FHA method is accurate for power calculations, it introduces notable errors in ZVS analysis due to the high-order harmonics. Therefore, it is important to consider the high-order harmonics in i_{Lf1} and i_{Lf2} . Owing to the filtering effects of L_{f1} , C_{f1} , L_{f2} , and C_{f2} , the voltages across C_{f1} and C_{f2} (denoted as u_{Cf1} and u_{Cf2}) contain little high-order harmonics [13]. Hence, the calculations of u_{Cf1} and u_{Cf2} can still be achieved using the FHA method. Specifically, the expressions of u_{Cf1} and u_{Cf2} are as follows:

$$u_{Cf1}(t) = \frac{4\alpha V_1}{\pi} \sin\left(\frac{D_P\pi}{2}\right) \sin(\omega t) + \frac{4MV_2}{\pi L_{f2}} \sin\left(\frac{D_S\pi}{2}\right) \times \sin(\omega t - \pi/2 - \Delta\delta) \quad (13)$$

$$u_{Cf2}(t) = \frac{4MV_1}{\pi L_{f1}} \sin\left(\frac{D_P\pi}{2}\right) \sin(\omega t) + \frac{4\beta V_2}{\pi} \sin\left(\frac{D_S\pi}{2}\right) \times \sin(\omega t - \pi/2 - \Delta\delta). \quad (14)$$

Applying KVL based on Fig. 1 and ignoring the loss resistances, the following differential equations are obtained as:

$$v_{ab} - u_{Cf1} = L_{f1} \frac{di_{Lf1}}{dt}, u_{Cf2} - v_{cd} = L_{f2} \frac{di_{Lf2}}{dt}. \quad (15)$$

By solving (15), the time-domain expressions of $i_{Lf1}(t)$ and $i_{Lf2}(t)$ can be obtained.

Using $i_{Lf1}(t)$ as an illustrative example, examination of Fig. 2 reveals that the inverter output voltage v_{ab} remains constant at V_1 during the time interval $t_{P0} < t < t_{P1}$. Within this interval, the expression for $i_{Lf1}(t)$ can be derived as follows:

$$i_{Lf1}(t) = i_{Lf1}(t_{P0}) + \frac{1}{L_{f1}} \int_{t_{P0}}^t [V_1 - u_{Cf1}(\tau)] d\tau. \quad (16)$$

Moreover, v_{ab} remains at 0 during the period $t_{P1} < t < t_{P2}$, within which the expression for $i_{Lf1}(t)$ can be derived as

$$i_{Lf1}(t) = i_{Lf1}(t_{P1}) + \frac{1}{L_{f1}} \int_{t_{P1}}^t [-u_{Cf1}(\tau)] d\tau. \quad (17)$$

Given the symmetrical characteristics of the current waveforms, it is apparent that $i_{Lf1}(t_{P0}) = -i_{Lf1}(t_{P2})$. Consequently, the

derivation of $i_{Lf1}(t_{P0})$ is as follows:

$$i_{Lf1}(t_{P0}) = -\frac{V_1 D_P \pi}{2\omega L_{f1}} + \frac{4\alpha V_1}{\pi\omega L_{f1}} \sin^2\left(\frac{D_P\pi}{2}\right) + \frac{4MV_2}{\pi\omega L_{f1} L_{f2}} \sin\left(\frac{D_S\pi}{2}\right) \cos\left(\frac{D_P\pi}{2} + \Delta\delta\right). \quad (18)$$

The derivation of $i_{Lf2}(t_{S2})$ can be accomplished in a similar way, and it is expressed as

$$i_{Lf2}(t_{S2}) = -\frac{V_2 D_S \pi}{2\omega L_{f2}} + \frac{4\beta V_2}{\pi\omega L_{f2}} \sin^2\left(\frac{D_S\pi}{2}\right) + \frac{4MV_1}{\pi\omega L_{f1} L_{f2}} \sin\left(\frac{D_P\pi}{2}\right) \cos\left(\frac{D_S\pi}{2} + \Delta\delta\right). \quad (19)$$

Furthermore, substituting (18) into (12) yields the optimal α_{opt} for achieving the inverter ZVS, which is expressed as

$$\alpha_{opt} = \Gamma^{-1} \times [-2\pi\omega L_{f1} L_{f2} I_{ZVS} + V_1 L_{f2} D_P \pi^2 - 8MV_2 \sin(D_S\pi/2) \cos(D_P\pi/2 + \Delta\delta)] \quad (20)$$

where $\Gamma = 8V_1 L_{f2} \sin^2(D_P\pi/2)$. Similarly, substituting (19) into (12) obtains the optimal β_{opt} for rectifier ZVS, which is

$$\beta_{opt} = \Lambda^{-1} \times [-2\pi\omega L_{f1} L_{f2} I_{ZVS} + V_2 L_{f1} D_S \pi^2 - 8MV_1 \sin(D_P\pi/2) \cos(D_S\pi/2 + \Delta\delta)] \quad (21)$$

where $\Lambda = 8V_2 L_{f1} \sin^2(D_S\pi/2)$.

Based on the above analysis, it is evident that by dynamically adjusting α and β to α_{opt} and β_{opt} , optimal ZVS for both the inverter and rectifier can be achieved with minimal reactive power.

B. Power Regulation and Maximum Efficiency Tracking

Substituting (2) into (11) yields the output power expression of the proposed system

$$P_{out} = \frac{8V_1 V_2 M \sin(D_P\pi/2) \sin(D_S\pi/2) \sin(\delta)}{\omega\pi^2 L_{f1} L_{f2}}. \quad (22)$$

As evident from (22), power regulation can be achieved by adjusting D_P and D_S . However, there are multiple combinations of D_P and D_S that can achieve a given output power. Therefore, it is important to establish the optimal $D_P - D_S$ relationship to achieve maximum efficiency tracking. To determine the maximum efficiency point for the proposed system, the efficiency of the resonant circuits is derived as

$$\eta \approx \frac{\omega M L_{f1} L_{f2} |\sin(\delta)|}{AG_{AC} + B/G_{AC} + C} \quad (23)$$

where $A = [(\beta - 1)^2 R_{Lf2} + R_2] L_{f1}^2 + R_{Lf1} M^2$, $B = [(\alpha - 1)^2 R_{Lf1} + R_1] L_{f2}^2 + R_{Lf2} M^2$, and $C = 2M \sin(\Delta\delta) [(1 - \alpha) R_{Lf1} L_{f2} + (1 - \beta) R_{Lf2} L_{f1}] + \omega M L_{f1} L_{f2} |\sin(\delta)|$.

Analysis of (23) illustrates that the maximum efficiency of the resonant circuits is achieved when G_{AC} satisfy the following:

$$G_{AC_opt} = \sqrt{\frac{[(\alpha - 1)^2 R_{Lf1} + R_1] L_{f2}^2 + R_{Lf2} M^2}{[(\beta - 1)^2 R_{Lf2} + R_2] L_{f1}^2 + R_{Lf1} M^2}}. \quad (24)$$

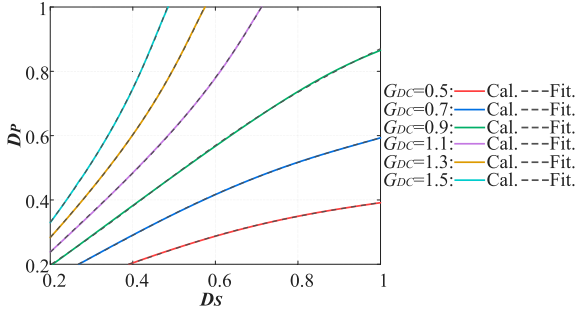


Fig. 7. Optimal relationship between D_P and D_S for maximum efficiency tracking.

Based on (2) and (24), there is an optimal relationship between D_P and D_S for maximum efficiency tracking. However, due to the limited computing power of microcontrollers, solving the optimal interrelationship between D_P and D_S in real time is difficult. Therefore, this article employs the approach of polynomial fitting to establish the optimal relationship between D_P and D_S , thereby achieving the maximum efficiency tracking.

With the parameters listed in Table II, the optimal relationship between D_P and D_S is constructed in Fig. 7. Within Fig. 7, the calculated outcomes are derived from (24), while the fitted results are generated through polynomial fitting applied to the calculated results. To ensure a satisfactory level of fitting accuracy, a third-order polynomial fit is adopted. It should be noted that when the WPT system operates in the boost mode ($G_{DC} > 1$), the duty cycle D_P exceeds D_S over the whole power range. To prevent output saturation of the controller, it is preferable to consider D_S as the independent variable in the boost mode, while regarding D_P as the dependent variable. The corresponding fitting relationship for the boost mode is as follows:

$$D_P = h_1 D_S^3 + h_2 D_S^2 + h_3 D_S + h_4. \quad (25)$$

Conversely, when the system works in the buck mode ($G_{DC} < 1$), the duty cycle D_S is always greater than D_P . Hence, the fitting expression for the buck mode can be given by

$$D_S = h_1 D_P^3 + h_2 D_P^2 + h_3 D_P + h_4. \quad (26)$$

C. Reduction of the Inductor RMS Currents

To illustrate the effectiveness of the proposed method at wide output voltages, Fig. 8 presents its performance in the buck mode with the dc voltage gain at $G_{DC} = 0.5$. To achieve dual-side ZVS, the compensation angle $\Delta\delta$ is selected as the maximum value of $\Delta\delta_P$ and $\Delta\delta_S$. Additionally, as shown in Fig. 8(a), the value of β is adjusted as the output power varies. The dynamic tuning of the secondary-side SCC minimizes excessive reactive power caused by the compensation angle $\Delta\delta$, thereby reducing the rms value of $i_{L_{f2}}$. Fig. 8(b) compares the rms value of $i_{L_{f2}}$ with and without capacitor tuning. As evident from Fig. 8(b), the introduction of SCC tuning contributes to a notable reduction in $I_{L_{f2}}$. This reduction not only decreases power losses in the inductor L_{f2} but also lowers the

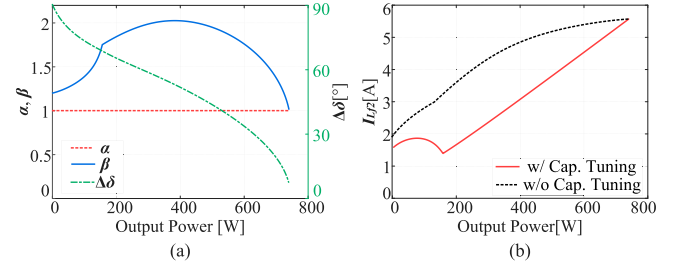


Fig. 8. Performance of the proposed method in the buck mode ($G_{DC} = 0.5$): (a) variations of α , β and $\Delta\delta$; and (b) comparison of $I_{L_{f2}}$ with and without capacitor tuning.

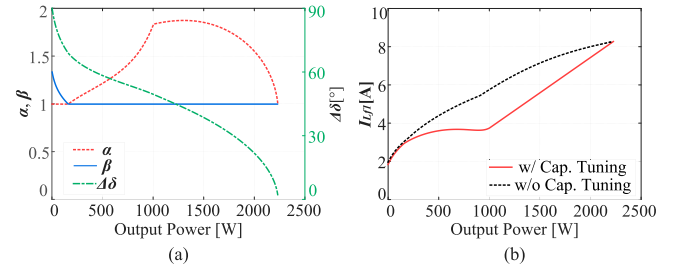


Fig. 9. Performance of the proposed method in the boost mode ($G_{DC} = 1.5$): (a) variations of α , β and $\Delta\delta$; and (b) comparison of $I_{L_{f1}}$ with and without capacitor tuning.

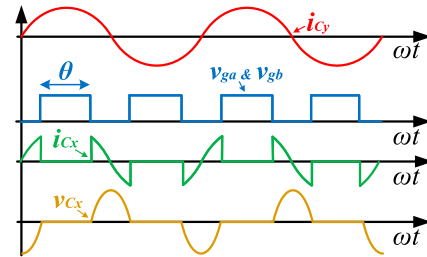


Fig. 10. Typical operating waveforms of the adopted SCCs.

conduction and turn-OFF losses for the rectifier, thus improving the overall efficiency.

Furthermore, Fig. 9 demonstrates the performance of the proposed approach in the boost mode with the dc voltage gain at $G_{DC} = 1.5$. By dynamically tuning α in the boost mode, as shown in Fig. 9, the rms value of $i_{L_{f2}}$ is reduced within a wide power range, leading to decreased power losses in the inductor L_{f1} , as well as reduced conduction and turn-OFF losses for the inverter.

D. Design and Implementation of SCCs

The operating waveforms of the adopted SCCs are shown in Fig. 10. According to [25], the equivalent capacitance of the adopted SCCs can be derived as

$$C_{eq} = \frac{\pi C_x C_y}{\pi C_x + [\pi - \theta - \sin(\theta)] C_y}. \quad (27)$$

Considering the tuning range of α and β , the compensation capacitances C_{x1} and C_{y1} of the primary SCC are designed as

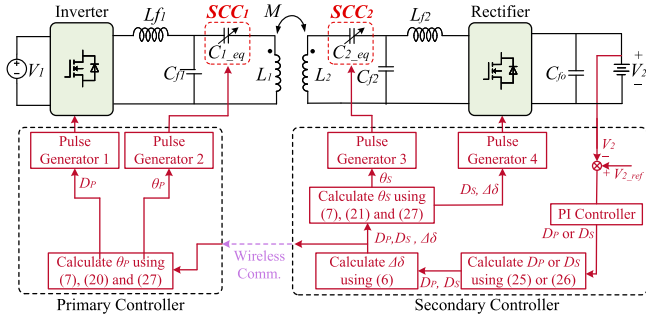


Fig. 11. Control block diagram of the proposed WPT system.

36.3 and 24.9 nF, while C_{x2} and C_{y2} of the secondary SCC are designed as 36.3 and 78 nF, respectively. With the designed parameters, the relationship between α and θ_P , as well as the relationship between β and θ_S , can be obtained by combining (7) and (27). Moreover, according to the simulation results, the maximum current and voltage stresses across the SCC switches are 13.1 A and 662.9 V, respectively. Notably, when selecting the current and voltage ratings for the SCC switches, sufficient margins should be considered. In our developed prototype, the MOSFETs (GeneSic G3R20MT12K) available in our laboratory are adopted as the SCC switches. Moreover, based on the measured maximum coil current (13.4 A) in the experiments and the ON-resistance (20 m Ω) of the adopted SCC MOSFETs, the maximum voltage drop caused by the SCC switches is calculated as 0.54 V. Compared with the voltage stresses of inductors and capacitors within the resonant circuits, which can reach hundreds of volts, the maximum voltage drop of 0.54 V is negligible.

It is noteworthy that although introducing SCC increases hardware costs, this notably improves the overall efficiency of the system. The improved efficiency not only conserves energy but also alleviates thermal stress on the converters and inductors. Hence, for applications demanding high energy efficiency, the proposed method is beneficial.

E. Control Framework

Fig. 11 presents the control block diagram of the proposed WPT system. First, the dc output voltage is measured by a voltage sensor. Subsequently, a proportional-integral (PI) controller is employed for voltage tracking. The output of the PI controller depends on the input-to-output dc voltage gain (G_{DC}) of the system. When the system operates in the boost mode, the output of the PI controller defines the rectifier duty cycle D_S , while the inverter duty cycle D_P is calculated by (25). Conversely, if the system works in the buck mode, the PI controller generates D_P , with D_S determined by (26). After the duty cycles D_P and D_S are obtained, the compensation angle $\Delta\delta$ is calculated by (6) to implement ZVS for both the inverter and rectifier. Additionally, the SCC control angles θ_P and θ_S are also derived and applied to the dual-side SCCs to enable dynamic capacitor tuning, thereby reducing the inductor currents and minimizing turn-OFF currents for the converters.

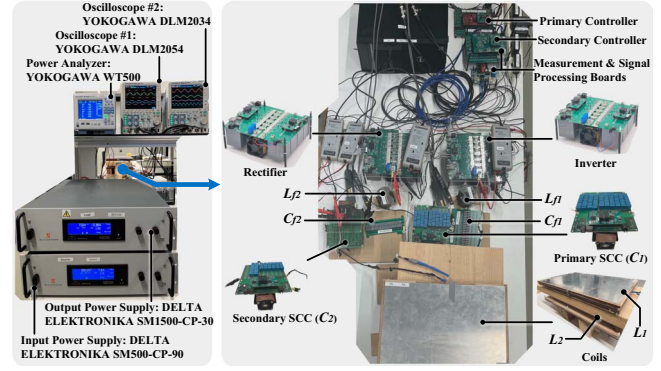


Fig. 12. Experimental setup.

TABLE III
SPECIFICATIONS OF THE REFERENCE DESIGN AND THE SCALE-DOWN PROTOTYPE

Symbol	Specifications	Reference Design ¹	Scale-Down Prototype
P_R	Rated power	7.7 kW	2.0 kW
V_1	DC input voltage	600 V	300 V
V_2	DC output voltage	300–900 V	150–450 V
I_R	Rated charging current	9.0 A	4.5 A
f_s	Switching frequency	85 kHz	85 kHz

Note: ¹The reference design is based on the SAE J2954 standard [26].

Notably, in practical EV charging scenarios, the reference output voltage (V_{2_ref}) can be regulated according to various battery voltages and the required charging profile. By implementing the PI controller to adjust D_P and D_S , the dc output voltage can be regulated to V_{2_ref} . Depending on the relationship between the dc input voltage (V_1) and V_{2_ref} , the proposed system operates either in the buck or boost modes. Specifically, when V_{2_ref} is configured to be lower than V_1 , the proposed system operates in the buck mode; conversely, when V_{2_ref} is larger than V_1 , the proposed system works in the boost mode.

IV. EXPERIMENTAL VERIFICATIONS

A. Experimental Platform

To demonstrate the effectiveness of the proposed method, a 2.0-kW scale-down WPT prototype with a reconfigurable DLCC topology was developed, as shown in Fig. 12. The configurations of dc voltages and rated power of the scale-down prototype are based on the reference design recommended in SAEJ 2954 standard [26], as illustrated in Table III. For the reference design, the 600 V dc input voltage can be provided by a front-end power factor correction (PFC) converter, while 300–900 V dc output voltage accommodates most EV battery voltages, according to Table I. Based on the reference design, the dc voltages of the developed prototype are scaled down by a factor of 0.5. Notably, the application of the proposed method is suited for residential wireless EV charging, where

the battery charging current is relatively low, and the thermal issue of batteries is not a significant concern. Moreover, this prototype utilizes two H-bridge converters as the inverter and rectifier stages, with two separate SCCs on the primary and secondary sides, respectively. The entire system was powered by a constant 300-V dc source, with a bidirectional dc power supply serving as an electronic load. The control algorithm and pulse generation were implemented through TI Launchpads F28379D. To achieve ZVS for the power switches, the designed minimum ZVS current was set to 2 A. It is noteworthy that in the proposed method, the control variables need to be transmitted from the secondary to the primary. Additionally, the primary circuit parameters may need to be transmitted to the secondary controller in practice. Hence, wireless communication between the primary and secondary sides is essential. In the prototype, the nRF24L01+ module is used to achieve dual-side information exchange. More detailed parameters of the prototype are illustrated in Table II.

B. Steady-State Operating Waveforms

Fig. 13 presents the steady-state operating waveforms of the proposed method in the boost mode. Here, the output voltage is adjusted at 450 V with a dc voltage gain of $G_{DC} = 1.5$. As demonstrated in Fig. 13, the proposed method simultaneously adjusts the inverter and rectifier duty cycles (D_P and D_S), as well as the phase difference between v_{ab} and v_{cd} (δ), to achieve power regulation, ZVS operations, and maximum efficiency tracking under load variations. More importantly, the primary-side SCC is dynamically regulated in the boost mode. Fig. 13 also displays the operating waveforms of the primary-side SCC (see the waveforms of v_{cx1} and v_{gs_sa1}). As it can be observed, the SCC consistently achieves ZVS turn-ON and turn-OFF under power variations, thus reducing the switching losses of the SCC MOSFETs. Additionally, thanks to the dynamic capacitor tuning, the ZVS of both the inverter and rectifier is achieved with minimized ZVS current. As illustrated in Fig. 13, the minimum ZVS currents for both the inverter and rectifier are regulated at around the designed value of 2 A.

Moreover, the steady-state operating waveforms of the proposed method in the buck mode, where the output voltage is regulated to 150 V with a dc voltage gain at $G_{DC} = 0.5$, is further demonstrated in Fig. 14. To minimize the reactive power in the buck mode, the secondary-side SCC is dynamically adjusted. The secondary-side SCC achieves ZVS turn-ON and turn-OFF to lower the SCC switching losses as well. Meanwhile, the minimum ZVS current for both the inverter and rectifier is also tuned to approximately 2 A.

C. Benchmark With TPS

To illustrate the enhanced efficiency achieved by the proposed method, the operating waveforms and measured dc-to-dc efficiency of the proposed method are benchmarked with the existing TPS method, as shown in Figs. 15 and 16.

When delivering 1-kW power in the boost mode ($V_2 = 450$ V, $G_{DC} = 1.5$), as shown in Fig. 15(a), the rms value of $i_{L_{f1}}$ reaches 6.5 A under the TPS control, while the minimum ZVS

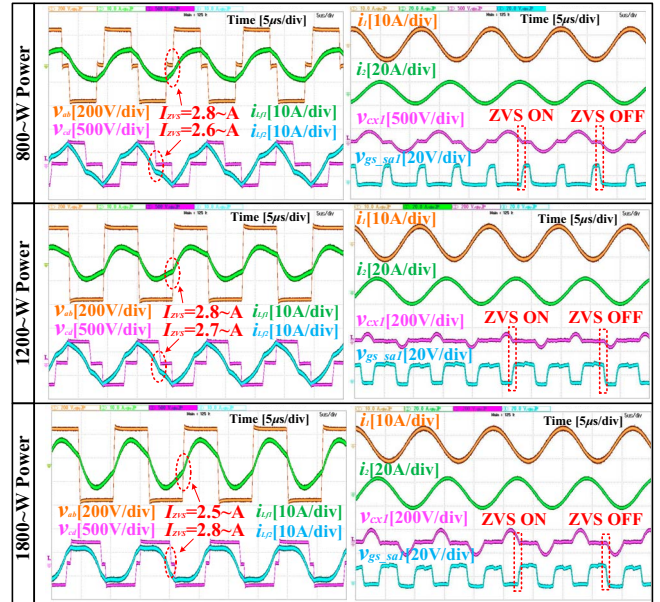


Fig. 13. Steady-state operating waveforms of the proposed method when delivering various power in boost mode ($V_2 = 450$ V, $G_{DC} = 1.5$).

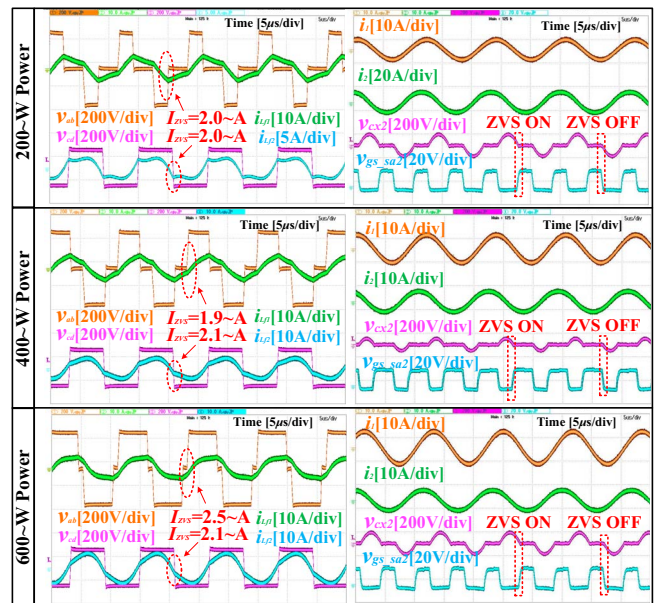


Fig. 14. Steady-state operating waveforms of the proposed method when delivering various power in buck mode ($V_2 = 150$ V, $G_{DC} = 0.5$).

current of the inverter reaches up to 9.2 A. However, owing to the dynamic tuning of the primary-side SCC, as shown in Fig. 15(b), the rms value of $i_{L_{f1}}$ is reduced from 6.5 to 4.2 A in the proposed method, and the minimum ZVS current of the inverter is decreased from 9.2 to 2.8 A. Consequently, the efficiency is improved from 92.7% to 94.5% in the proposed method, resulting in an efficiency improvement of up to 1.8%. Fig. 16 further presents the comparisons in the buck mode ($V_2 = 150$ V, $G_{DC} = 0.5$). With active tuning of the secondary-side SCC, the proposed method reduces the rms value of $i_{L_{f2}}$

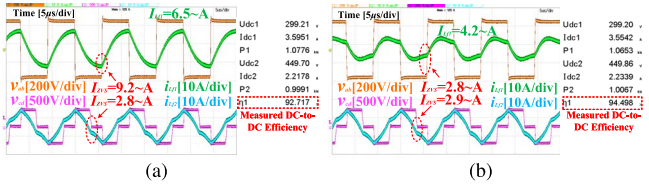


Fig. 15. Benchmark when delivering 1-kW power in the boost mode ($V_2 = 450$ V, $G_{DC} = 1.5$): operating waveforms and measured dc-to-dc efficiency of (a) TPS method and (b) proposed method.

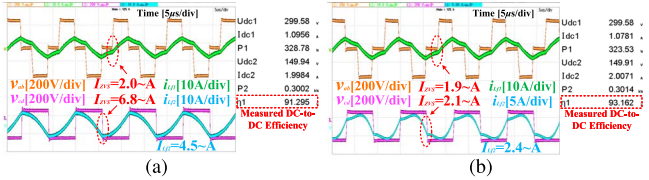


Fig. 16. Benchmark when delivering 300-W power in the boost mode ($V_2 = 150$ V, $G_{DC} = 0.5$): operating waveforms and measured dc-to-dc efficiency of (a) TPS method and (b) proposed method.

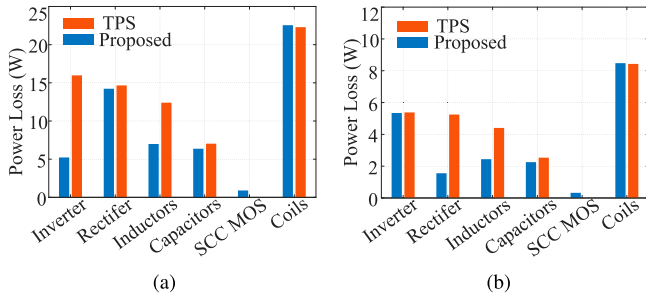


Fig. 17. Calculated power loss breakdown for the proposed method and the conventional TPS method: (a) when delivering 1 kW in the boost mode; and (b) when delivering 300 W in the buck mode.

from 4.5 to 2.4 A when delivering 300 W. Also, it decreases the minimum rectifier ZVS current from 6.8 to 2.1 A. This results in an efficiency improvement of up to 1.9%, with the efficiency improved from 91.3% to 93.2%.

Moreover, Fig. 17 demonstrates the calculated power loss breakdown for the above experiments. As shown in Fig. 17(a), when operating in the boost mode, the proposed method significantly reduces both the inverter and inductor losses. These loss reductions result from the decreased primary inductor current and inverter turn-OFF currents. Meanwhile, the losses of the rectifier, capacitors, and coils exhibit similar performance in both methods. Conversely, as shown in Fig. 17(b), the proposed method notably decreases the rectifier and inductor losses by reducing the secondary inductor current and rectifier turn-OFF currents in the buck mode. In this case, the losses of the inverter, capacitors, and coils are similar. Notably, due to the low ON-resistance of SCC MOSFETs and the implementation of zero-voltage turn-ON and turn-OFF for SCC switches, the extra losses caused by the SCC MOSFETs are not significant in both the boost and buck modes.

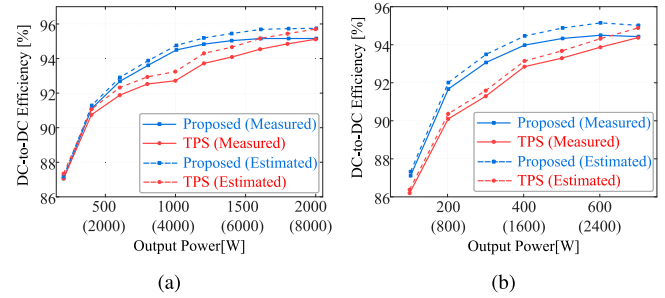


Fig. 18. Efficiency comparisons between the proposed method and the TPS method under various output power levels: (a) in the boost mode ($G_{DC} = 1.5$); and (b) in the buck mode ($G_{DC} = 0.5$). Here, the measured efficiency in experiments is shown with solid lines, while the estimated efficiency for the reference system is indicated by dotted lines. The measured power range of the scale-down prototype is [200, 2000] and [100, 700] W for the boost and buck modes, while the estimated power range of the reference system is [800, 8000] and [400, 2800] W for the boost and buck modes, respectively.

Furthermore, the measured dc-dc efficiency of the proposed scheme is evaluated in comparison with the TPS method across various output power levels, as visualized in Fig. 18. It demonstrates that the proposed method enhances the efficiency over a broad output power, achieving a maximum efficiency improvement of 1.8% in the boost mode and 1.9% in the buck mode. Additionally, the estimated efficiency of the reference system (listed in Table III) is illustrated in Fig. 18 as well. The estimated efficiency provides a reference for assessing efficiency performance in practical setups.

To validate the feasibility of the proposed approach for EV battery charging, experiments are further carried out under CC and constant voltage (CV) modes. As shown in Fig. 19, the proposed approach is able to implement CC and CV charging profiles under both the boost and buck modes, achieving a peak efficiency of 95.16% (in the boost mode) and 94.5% (in the buck mode), respectively.

D. Transient Response

To demonstrate the feasibility of the proposed method in practical EV charging applications, the transient response capability of this method is evaluated. Here, the dc output voltage is measured utilizing the signal measurement & processing boards, while a PI controller is employed for CV tracking.

Fig. 20(a) shows the dynamic performance of the proposed method when the equivalent dc load is increased from 250 to 150 Ω in the boost mode. As it can be observed, the output voltage is reliably controlled at 450 V under load changes, with the response time at 72 ms. Moreover, Fig. 20(b) presents the dynamic performance in the buck mode. Experiments reveal that the proposed method restores the output voltage within 110 ms when the dc load is reduced from 50 to 100 Ω .

E. Comparisons With Other Existing Control Methods

Table IV demonstrates the comparisons between the proposed approach and other existing methods. As it can be observed, although [19], [20], [21] also incorporated

TABLE IV
COMPARISONS WITH OTHER EXISTING CONTROL METHODS

Ref.	Comp.	Control Scheme ¹	Control Complexity	Control Objectives	Wide Output Voltages Considering Buck and Boost Modes	Rated Power	Peak DC-DC Efficiency
[19]	DLCC	Dual-side SCCs & the inverter control	Gradient descent algorithm and PI	Compensating for self-inductance variations	No	3.0 kW	91.5%
[20]	SS	Dual-side SCCs & the inverter control	Hill-climbing and linear search algorithms	Compensating for self-inductance variations	No	500 W	85.8%
[21]	SS	Dual-side SCCs & the inverter control	Perturb & observe algorithm and PI	Compensating for self-inductance variations	No	1.0 kW	91.49%
[13]	DLCC	The inverter + rectifier control	Calculations	Wide power regulation & dual-side ZVS	No	1.0 kW	94.83%
[22]	LCC-S	Primary SCC & the inverter control	PI and calculations	Wide power regulation & inverter ZVS	No	500 W	94.7%
[23]	DLCC	Secondary SCC & the inverter control	PI and calculations	Wide power regulation & inverter ZVS	No	700 W	91.0%
[24]	DLCC	Primary SCC & the inverter + rectifier control	PI and calculations	Wide power regulation & dual-side ZVS	No	1.6 kW	92.3%
This work	DLCC	Dual-side SCCs & the inverter + rectifier control	PI and calculations	Wide power regulation & dual-side optimal ZVS	Yes	2.0 kW	95.16%

Note: ¹The diode rectifier was utilized in the inverter control, while the active rectifier was employed within the inverter + rectifier control.

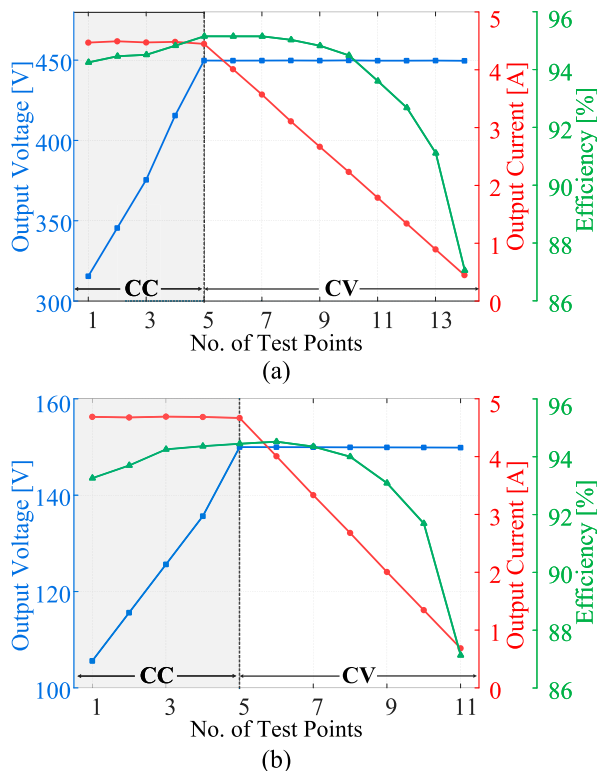


Fig. 19. Implementation of CC-CV charging profile in the experiments: (a) in the boost mode; and (b) in the buck mode.

dual-side SCC tuning, their main focus is to compensate for self-inductance variations under considerable coil misalignment. On the other hand, previous studies in [13], [22], [23],

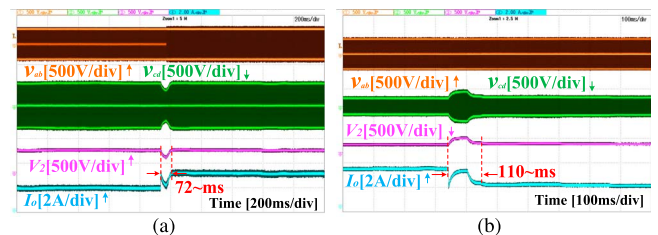


Fig. 20. Transient response of the proposed method: (a) when the equivalent dc load is increased from 250 to 150 Ω ($V_2 = 450$ V); (b) when the equivalent dc load is reduced from 50 to 100 Ω ($V_2 = 150$ V).

and [24] have explored achieving wide output power regulation and ZVS implementation. However, the existing TPS method in [13] leads to significant reactive power at wide output voltages. Additionally, the authors [22], [23] only implemented the inverter control, whereas a diode rectifier was employed on the secondary side. This leads to a limited power regulation range when compared with the dual-side control. Moreover, in [22], [23], and [24], the SCC was solely implemented on one side (either the primary or secondary), and only the inverter ZVS was optimized in these methods.

Compared with other existing methods, the proposed method aims to achieve wide power regulation and efficiency optimization while accommodating wide output voltages, considering both the buck and boost modes. Through investigating the TPS method for asymmetric DLCC topology across wide output voltages, the limitations of this method are identified. In the proposed method, dual-side SCC tuning is introduced to enable optimal ZVS for both the inverter and rectifier. This notably reduces the rms values of the inductor currents and minimizes

the ZVS currents for the converter switches. Moreover, through the cooperative control of the inverter, rectifier, and SCCs, the proposed method simultaneously achieves wide power regulation, dual-side optimal ZVS, and maximum efficiency tracking at wide output voltage variations.

Additionally, the control complexities of different methods are compared. As shown in Table IV, intelligent algorithms were employed to dynamically compensate for self-inductance variations in [19], [20], and [21], encompassing the gradient descent algorithm [19], the hill-climbing and linear search algorithms [20], as well as the perturb & observe algorithm [21]. On the other hand, calculations were performed to achieve wide power regulation and ZVS in [13]; however, closed-loop control was not demonstrated. In [22], [23], and [24], a PI controller was further introduced to achieve closed-loop control. Compared with existing approaches, the proposed method utilizes one PI controller for the output voltage control. Moreover, fundamental calculations are performed to enable dual-side optimal ZVS and maximum efficiency tracking. These calculations only involve arithmetic and trigonometric operations, which do not significantly increase the computation complexity and can be easily managed by the microcontrollers.

V. CONCLUSION

In this article, a dual-side cooperative control strategy has been proposed for wireless EV charging applications to optimize efficiency over a wide range of output voltage. The proposed method integrates two separate SCCs into the DLCC topology to mitigate the increased reactive power during the significant variation of the dc output voltage. Based on the dual-side capacitor tuning, this approach notably reduces the inductor rms currents and minimizes turn-OFF currents for the converters, thereby improving efficiency across a broad range of output power and voltage. Experimental results demonstrated that the proposed method achieves a higher efficiency compared with the existing TPS method in both the buck and boost modes.

REFERENCES

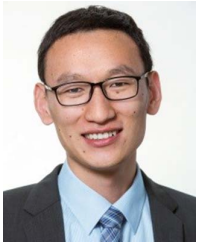
- [1] M. Amjad, M. Farooq-i Azam, Q. Ni, M. Dong, and E. A. Ansari, "Wireless charging systems for electric vehicles," *Renewable Sustain. Energy Rev.*, vol. 167, 2022, Art. no. 112730.
- [2] W. Shi, J. Dong, T. B. Soeiro, C. Riekerk, F. Grazian, G. Yu, and P. Bauer, "Design of a highly efficient 20-kW inductive power transfer system with improved misalignment performance," *IEEE Trans. Transp. Electric.*, vol. 8, no. 2, pp. 2384–2399, Jun. 2022.
- [3] A. Mostafa et al., "Output power regulation of a series-series inductive power transfer system based on hybrid voltage and frequency tuning method for electric vehicle charging," *IEEE Trans. Ind. Electron.*, vol. 69, no. 10, pp. 9927–9937, Oct. 2022.
- [4] F. Grazian, T. B. Soeiro, and P. Bauer, "Voltage/current doubler converter for an efficient wireless charging of electric vehicles with 400-v and 800-v battery voltages," *IEEE Trans. Ind. Electron.*, vol. 70, no. 8, pp. 7891–7903, Aug. 2023.
- [5] EVSpecifications: specifications, news and comparisons, Accessed: Apr. 9, 2024. [Online]. Available: www.evspecifications.com
- [6] "Sophisticated thermal management, up to 800-volt system voltage." Accessed: Apr. 9, 2024. [Online]. Available: media.porsche.com/mediakit/taycan/en/porsche-taycan/die-batterie
- [7] Z. Zhou, L. Zhang, Z. Liu, Q. Chen, R. Long, and H. Su, "Model predictive control for the receiving-side dc-dc converter of dynamic wireless power transfer," *IEEE Trans. Power Electron.*, vol. 35, no. 9, pp. 8985–8997, Sep. 2020.
- [8] G. Yu, J. Dong, T. B. Soeiro, G. Zhu, Y. Yao, and P. Bauer, "Three-mode variable-frequency ZVS modulation for four-switch buck+ boost converters with ultra-high efficiency," *IEEE Trans. Power Electron.*, vol. 38, no. 4, pp. 4805–4819, Apr. 2023.
- [9] Z. Hua, K. Chau, W. Han, W. Liu, and T. W. Ching, "Output-controllable efficiency-optimized wireless power transfer using hybrid modulation," *IEEE Trans. Ind. Electron.*, vol. 69, no. 5, pp. 4627–4636, May 2022.
- [10] V. Yenil and S. Cetin, "An improved pulse density modulation control for secondary side controlled wireless power transfer system using LCC-S compensation," *IEEE Trans. Ind. Electron.*, vol. 69, no. 12, pp. 12762–12772, Dec. 2022.
- [11] S. Chen, H. Li, and Y. Tang, "Extending the operating region of inductive power transfer systems through dual-side cooperative control," *IEEE Trans. Ind. Electron.*, vol. 67, no. 11, pp. 9302–9312, Nov. 2020.
- [12] Y. Li, J. Hu, F. Chen, Z. Li, Z. He, and R. Mai, "Dual-phase-shift control scheme with current-stress and efficiency optimization for wireless power transfer systems," *IEEE Trans. Circuits Syst. I: Reg. Papers*, vol. 65, no. 9, pp. 3110–3121, Sep. 2018.
- [13] X. Zhang et al., "A control strategy for efficiency optimization and wide ZVS operation range in bidirectional inductive power transfer system," *IEEE Trans. Ind. Electron.*, vol. 66, no. 8, pp. 5958–5969, Aug. 2019.
- [14] Y. Li, W. Sun, X. Zhu, and J. Hu, "A hybrid modulation control for wireless power transfer systems to improve efficiency under light-load conditions," *IEEE Trans. Ind. Electron.*, vol. 69, no. 7, pp. 6870–6880, Jul. 2022.
- [15] G. Zhu, J. Dong, W. Shi, T. B. Soeiro, J. Xu, and P. Bauer, "A mode-switching-based phase shift control for optimized efficiency and wide ZVS operations in wireless power transfer systems," *IEEE Trans. Power Electron.*, vol. 38, no. 4, pp. 5561–5575, Apr. 2023.
- [16] X. Zhang, J. Li, and X. Tong, "A unique design approach of double-sided LCC compensated IPT system for misalignment-tolerant characteristic," *IEEE Trans. Power Electron.*, vol. 38, no. 1, pp. 1288–1300, Jan. 2023.
- [17] S. Luo, Z. Yao, Z. Zhang, X. Zhang, and H. Ma, "Balanced dual-side LCC compensation in IPT systems implementing unity power factor for wide load range and misalignment tolerance," *IEEE Trans. Ind. Electron.*, vol. 70, no. 8, pp. 7796–7809, Aug. 2023.
- [18] J. Huang, X. He, P. Huo, and R. Xu, "A hybrid modulation strategy for LCC-LCC compensated bidirectional wireless power transfer system to achieve high efficiency in the whole operating range," *IEEE Trans. Ind. Electron.*, vol. 71, no. 1, pp. 327–337, Jan. 2024.
- [19] Z. Luo, Y. Zhao, M. Xiong, X. Wei, and H. Dai, "A self-tuning LCC-LCC system based on switch-controlled capacitors for constant-power wireless electric vehicle charging," *IEEE Trans. Ind. Electron.*, vol. 70, no. 1, pp. 709–720, Jan. 2023.
- [20] W. Li, Q. Zhang, C. Cui, and G. Wei, "A self-tuning S/S compensation WPT system without parameter recognition," *IEEE Trans. Ind. Electron.*, vol. 69, no. 7, pp. 6741–6750, Jul. 2022.
- [21] R. Matsumoto, T. Fujita, and H. Fujimoto, "Communication-less reactance compensation using PWM-controlled switched capacitors for wireless power transfer," *IEEE Trans. Power Electron.*, vol. 38, no. 10, pp. 13194–13206, Oct. 2023.
- [22] X. Wang, J. Xu, M. Leng, H. Ma, and S. He, "A hybrid control strategy of LCC-S compensated WPT system for wide output voltage and ZVS range with minimized reactive current," *IEEE Trans. Ind. Electron.*, vol. 68, no. 9, pp. 7908–7920, Sep. 2021.
- [23] L. Zhou, R. Mai, S. Liu, J. Yu, Y. Li, and L. Fu, "Minimizing input current of the rectifier of LCC-LCC compensated IPT systems by switch-controlled capacitor for improving efficiency," *IEEE Trans. Ind. Appl.*, vol. 58, no. 1, pp. 1010–1021, Jan./Feb. 2022.
- [24] N. Fu, J. Deng, Z. Wang, and D. Chen, "An LCC-LCC compensated WPT system with switch-controlled capacitor for improving efficiency at wide output voltages," *IEEE Trans. Power Electron.*, vol. 38, no. 7, pp. 9183–9194, Jul. 2023.
- [25] F. Grazian, T. B. Soeiro, and P. Bauer, "Inductive power transfer based on variable compensation capacitance to achieve an EV charging profile with constant optimum load," *IEEE J. Emerg. Sel. Topics Power Electron.*, vol. 11, no. 1, pp. 1230–1244, Feb. 2023.

- [26] *Wireless Power Transfer for Light-Duty Plug-in/Electric Vehicles and Alignment Methodology*, SAE J2954 standard. Accessed: Apr. 9, 2024. [Online]. Available: www.sae.org/standards/content/j2954_202010/



Gangwei Zhu (Graduate Student Member, IEEE) received the B.S. degree from Central South University, Changsha, China, in 2018, and the M.S. degree from Shanghai Jiao Tong University, Shanghai, China, in 2021. He is currently working toward the Ph.D. degree from Delft University of Technology, Delft, The Netherlands, all in electrical engineering.

His research interests include design, modeling, and control for power electronics and wireless power transfer.



Jianning Dong (Senior Member, IEEE) received the B.S. and Ph.D. degrees in electrical engineering from the Southeast University, Nanjing, China, in 2010 and 2015, respectively.

Since 2016, he has been an Assistant Professor with the DC System, Energy Conversion and Storage (DCE&S) Group, Delft University of Technology (TU Delft), Delft, The Netherlands. He was a Postdoctoral Researcher with McMaster Automotive Resource Centre, McMaster University, Hamilton, ON, Canada. His research

interests include electromechanical energy conversion and contactless power transfer.



Thiago Batista Soeiro (Senior Member, IEEE) received the M.Sc. degree from the Federal University of Santa Catarina, Florianopolis, Brazil, in 2007, and the Ph.D. degree from Swiss Federal Institute of Technology, Zurich, Switzerland, in 2012, both in electrical engineering.

Since 2022, he has been a Full Professor in power electronics with the Power Electronics Group, University of Twente, Enschede, The Netherlands. From 2012 to 2013, he was a Researcher with the Power Electronics Institute,

Federal University of Santa Catarina. From 2013 to 2018, he was a Senior Scientist with the Corporate Research Center, ABB Switzerland Ltd., Baden-Dattwil, Switzerland. From 2018 to 2022, he was an Associate Professor with the DC Systems, Energy Conversion and Storage Group, Delft University of Technology, Delft, The Netherlands. From January to October 2022, he was with the Power Management and Distribution Section for the European Space Research and Technology Centre, Noordwijk, The Netherlands.



Hani Vahedi (Senior Member, IEEE) received the Ph.D. (Hons.) degree in electrical engineering from École de Technologie Supérieure (ÉTS), University of Quebec, Montreal, QC, Canada, in 2016. After seven years of experience in industry as a Power Electronics Designer and the Chief Scientific Officer, he joined Delft University of Technology (TU Delft), where he is currently an Assistant Professor with the DCE&S group, working toward the electrification of industrial processes for clean energy transition.

He is the Technical Lead of Green Village 24/7 Energy Hub, TU Delft, implementing a local microgrid with green energy resources and a hydrogen energy storage system as the future of the energy systems. His research interests include multilevel converter topologies, control,

and modulation techniques, and its applications in the electrification of industrial processes and clean energy transition, such as smart grids, renewable energy conversion, electric vehicle chargers, green hydrogen production (electrolyzers), and fuel-cell systems. He is the Inventor of the PUC5 converter, holds multiple U.S./world patents, and transferred that technology to the industry, where he developed the first bidirectional electric vehicle dc charger based on his invention. He has published more than 80 technical papers in IEEE conferences and Transactions. He published a book on Springer Nature and a book chapter in Elsevier.

Dr. Vahedi received the Best Ph.D. Thesis Award from ETS for the academic year of 2016–2017. He is a Co-Chair of the Student & Young Professionals (S&YP) Committee of the IEEE Industrial Electronics Society (IES). He is an Associate Editor of IEEE TRANSACTIONS ON INDUSTRIAL ELECTRONICS, IEEE OPEN JOURNAL OF THE INDUSTRIAL ELECTRONICS SOCIETY, and IEEE OPEN JOURNAL OF POWER ELECTRONICS.



Pavol Bauer (Senior Member, IEEE) received the master's degree from the Technical University of Kosice, Kosice, Slovakia, in 1985, and the Ph.D. degree from Delft University of Technology, Delft, The Netherlands, in 1995, both in electrical engineering.

He is currently a Full Professor with the Department of Electrical Sustainable Energy, and the Head of DC Systems, Energy Conversion and Storage Group, Delft University of Technology. He is a Professor with Brno University of

Technology, Brno, Czech Republic, and an Honorary Professor with the Politehnica University Timisoara, Timisoara, Romania. From 2002 to 2003, he was with KEMA (DNV GL), Arnhem, The Netherlands, on different projects related to power electronics applications in power systems. He has published over 180 journal articles and 450 conference papers in his field. He is the Author or a Co-Author of eight books, holds seven international patents, and has organized several tutorials at international conferences. He has worked on many projects for the industry concerning wind and wave energy; power electronic applications for power systems such as Smarttrafo; HVDC systems; projects for smart cities such as photovoltaic (PV) charging of electric vehicles, PV and storage integration, and contactless charging. He participated in several Leonardo da Vinci and H2020, as a Project Partner in Electric Mobility Europe EU projects (ELINA, INETELE, E-Pragmatic, Micact, Trolley 2.0, OSCD, P2P, and Progressus), and as a Coordinator in PEMCWebLab.com-Edipe, SustEner, and Eranet DCMICRO.

Prof. Bauer is the Former Chairman of Benelux IEEE Joint Industry Applications Society, Power Electronics and Power Engineering Society Chapter, the Chairman of the Power Electronics and Motion Control Council, a Member of the Executive Committee of European Power Electronics Association, and a Member of the International Steering Committee at numerous conferences.